Cerebral Cortex, October 2020;30: 5309–5321

doi: 10.1093/cercor/bhaa111
Advance Access Publication Date: 1 June 2020
Original Article

ORIGINAL ARTICLE

Spatiotemporal Integrity and Spontaneous Nonlinear Dynamic Properties of the Salience Network Revealed by Human Intracranial Electrophysiology: A Multicohort Replication

Anup Das[1] and Vinod Menon[1,2,3]

[1]Department of Psychiatry & Behavioral Sciences, Stanford University School of Medicine, Stanford, CA 94305, USA, [2]Department of Neurology & Neurological Sciences, Stanford University School of Medicine, Stanford, CA 94305, USA and [3]Stanford Neurosciences Institute, Stanford University School of Medicine, Stanford, CA 94305, USA

Address correspondence to Anup Das, 1070 Arastradero Rd., Stanford University, Stanford, CA 94305, USA. Email: a1das@stanford.edu; Vinod Menon, 401 Quarry Rd., Stanford University, Stanford, CA 94305, USA. Email: menon@stanford.edu

Abstract

The salience network (SN) plays a critical role in cognitive control and adaptive human behaviors, but its electrophysiological foundations and millisecond timescale dynamic temporal properties are poorly understood. Here, we use invasive intracranial EEG (iEEG) from multiple cohorts to investigate the neurophysiological underpinnings of the SN and identify dynamic temporal properties that distinguish it from the default mode network (DMN) and dorsolateral frontal–parietal network (FPN), two other large-scale brain networks that play important roles in human cognition. iEEG analysis of network interactions revealed that the anterior insula and anterior cingulate cortex, which together anchor the SN, had stronger intranetwork interactions with each other than cross-network interactions with the DMN and FPN. Analysis of directionality of information flow between the SN, DMN, and FPN revealed causal outflow hubs in the SN consistent with its role in fast temporal switching of network interactions. Analysis of regional iEEG temporal fluctuations revealed faster temporal dynamics and higher entropy of neural activity within the SN, compared to the DMN and FPN. Critically, these results were replicated across multiple cohorts. Our findings provide new insights into the neurophysiological basis of the SN, and more broadly, foundational mechanisms underlying the large-scale functional organization of the human brain.

Key words: causality, human intracranial EEG, multicohort replication, nonlinear dynamics, salience network

Introduction

The salience network (SN) is a large-scale brain network which plays an important role in cognitive control and adaptive behaviors (Menon and Uddin 2010). Noninvasive human functional magnetic resonance imaging (fMRI) studies have demonstrated SN involvement in detection and attentional capture of goal-relevant stimuli and facilitating efficient access to other large-scale brain networks across a wide range of cognitive tasks (Dosenbach et al. 2006, 2008; Sridharan et al. 2008; Menon and Uddin 2010; Cai et al. 2014). SN dysfunction is prominent in many psychiatric and neurological disorders, and lesions to the

anterior insula (AI) and anterior cingulate cortex (ACC) significantly impair cognitive function (Jilka et al. 2014; Sha et al. 2019). Despite its critical role in cognitive function and dysfunction (Menon 2011; Uddin 2015), the electrophysiological foundations of the SN and its dynamic temporal properties are poorly understood. This problem is confounded by the inherent difficulties of obtaining high-quality intracranial EEG (iEEG) data from multiple brain regions, and the even greater challenge of obtaining independent cohorts of iEEG data for examining reproducibility of findings (Parvizi and Kastner 2018). Here we address these challenges and investigate the neurophysiological underpinnings of the SN, identify dynamic temporal properties that distinguish it from other key networks involved in human cognition, and demonstrate, for the first time, replicability of findings across multiple cohorts and data acquisition sites.

The human brain is organized into distinct yet dynamically interacting large-scale functional networks (Bressler and Menon 2010; Power et al. 2011). Human fMRI studies have demonstrated that the SN has a functional organization that is distinct from the medial default mode network (DMN) and lateral frontal–parietal network (FPN), two other large-scale brain networks that play an important role in external stimulus-related cognition and monitoring internal mental processes (Menon 2011; Power et al. 2011). The intrinsic connectivity of these networks displays close correspondence with task-related coactivation patterns, and this correspondence has allowed intrinsic and task-related connectivity associated with these networks to be demarcated and studied under a common framework (Sridharan et al. 2008; Supekar and Menon 2012). Crucially, the AI and ACC nodes of the SN are among the most commonly activated brain regions in all of human fMRI-based neuroimaging research, and joint analysis of multiple tasks further reveal reliable activations in the AI and ACC across most cognitive domains, suggesting that they form a "core" task-set system (Dosenbach et al. 2006, 2008; Ouyang et al. 2008). While the SN has been extensively investigated using fMRI, its electrophysiological underpinnings, millisecond timescale dynamic temporal properties, and the intrinsic dynamical temporal properties that distinguish the SN from the DMN and FPN are not known as fMRI does not have the requisite temporal resolution.

Functional connectivity analysis of fMRI time series data using model-free approaches such as independent components analysis and model-based approaches such as seed-based analyses has demonstrated spatial segregation of these networks into anatomically distinct brain regions (Menon 2015a, 2015b). The AI and ACC nodes of the SN are distinct from the posterior cingulate cortex and precuneus (PCC/precuneus) nodes of the DMN and the middle frontal gyrus (MFG) and supramarginal gyrus (SMG) nodes of the FPN. Further, unlike the SN and FPN, the DMN is typically deactivated during behaviorally demanding tasks, and it plays a more distinct role in internal mental processes (Greicius et al. 2008; Dastjerdi et al. 2011). Despite significant progress in the characterization of the SN and its internetwork connectivity, based on the analysis of blood oxygenation level-dependent (BOLD) fMRI signals, the electrophysiological foundations remain unknown. In particular, the low temporal resolution of fMRI has precluded elucidation of the dynamic temporal properties and nonlinear dynamics underlying intra-SN and its cross-network interactions. iEEG recordings with adequate sampling of electrodes from multiple distinct brain regions of interest have the potential to address this gap (Miller et al. 2009; Dastjerdi et al. 2011; Watrous et al. 2013; Kucyi et al. 2018).

To thoroughly characterize the electrophysiological properties of the SN and demonstrate a neural basis for its distinctiveness from the DMN and FPN, we leveraged two independent iEEG datasets: 1) the Montreal Neurological Institute (MNI) (Frauscher et al. 2018) which contains recordings from 106 patients and 2) University of Pennsylvania Restoring Active Memory (UPENN-RAM) (Jacobs et al. 2016) containing recordings from 102 patients who underwent treatment for intractable epilepsy. In both the MNI and UPENN-RAM cohorts, we examined resting-state iEEG from patients with electrode placements in the AI and ACC spanning the SN, as well as electrodes spanning the DMN and FPN. The MNI cohort served as our primary cohort, while the UPENN-RAM cohort served as our replication cohort. Crucially, the extensive sampling of electrode placements in these two cohorts provided a unique opportunity not only to investigate dynamic interactions between multiple brain regions but also to determine the reproducibility of our findings.

Given the highly nonlinear nature of neural dynamics (Freeman 2000), we probed SN integrity and temporal dynamics using both conventional linear and novel nonlinear measures under the assumption that the later can better capture temporal features of interregional interactions than linear measures alone (Pereda et al. 2005). Furthermore, neural dynamics are highly variable, intermittent, and nonstationary processes (Menon et al. 1996) that are again best captured by nonlinear analytic procedures. We first determined whether intranetwork interactions of iEEG signals within the SN are distinct from its cross-network interactions with the DMN and FPN. We hypothesized that intranetwork temporal correlation between the AI and ACC nodes of the SN would be stronger than their cross-network interactions with electrodes in the DMN and FPN, thereby revealing distinctive electrophysiological signatures of SN integrity.

Second, we examined directionality of information flow between the SN, DMN, and FPN as regions whose activities are not instantaneously synchronized may interact via time-delayed causal influences. Noninvasive studies using fMRI have suggested that the SN has strong causal influences on other brain networks and is thought to play an important role in switching between the DMN and FPN (Sridharan et al. 2008). Surprisingly, higher causal influences of the AI node of the SN on multiple brain areas have also been reported in resting-state fMRI (Deshpande et al. 2011). However, it is unclear whether these results are an artifact of regional variations in hemodynamic response in BOLD signals or whether they truly reflect an underlying neuronal process. To address this challenge, we used phase transfer entropy (PTE) (Lobier et al. 2014) and tested the hypothesis that the AI and ACC nodes of the SN would act as causal outflow hubs in their interactions with the DMN and FPN.

Third, we examined the linear and nonlinear dynamic properties of electrophysiological activity within the AI and ACC nodes of the SN and contrasted them to DMN and FPN nodes. We estimated decorrelation times, which capture the interval in which past "memory" in the time series is lost. We hypothesized shorter decorrelation times in the AI and ACC underlying greater temporal flexibility of the SN in comparison to the DMN and FPN. We then used sample entropy to probe the nonlinear neuronal dynamics of regional iEEG activity (Richman and Moorman 2000) and predicted that SN iEEG signals would show faster temporal dynamics consistent with its hypothesized role in network switching dynamics (Sridharan et al. 2008). Finally, we demonstrate that the unique neurophysiological properties of the SN and its intranetwork and cross-network dynamic inter-

actions with the DMN and FPN are replicable across multiple cohorts.

Materials and Methods

MNI iEEG Cohort

iEEG data from 106 patients shared by Gotman and colleagues at the Montreal Neurological Institute (MNI) were used as the primary cohort (Frauscher et al. 2018). iEEG recordings were downloaded from the MNI iEEG atlas website (MNI Open iEEG Atlas—Document Repository. URL: http://mni-open-ieegatlas.research.mcgill.ca). iEEG data were acquired from patients undergoing clinical evaluation for epilepsy surgery at the Montreal Neurological Institute (MNI) and associated hospitals Centre Hospitalier de l'Université de Montréal (CHUM) and Grenoble-Alpes University Hospital (CHUGA). All experimental procedures were acquired with informed consent with ethical guidelines and protocols administered by the MNI (Frauscher et al. 2018). Details of all the recordings sessions and data preprocessing procedures are described by Gotman and colleagues (Frauscher et al. 2018). Briefly, the MNI atlas consists of 60-s curated artifact-free iEEG data acquired in an "eyes closed" resting wakefulness state using standardized experimental conditions. Data were acquired during seizure free periods with electrodes located in the gray matter of the brain and outside the seizure onset zone. Peri-implantation CT/MRI images containing electrode locations were linearly registered to preimplantation MRI images for each patient, and these preimplantation MRI images were subsequently nonlinearly registered to the ICBM152 2009c nonlinear symmetric brain atlas to visualize the electrodes in stereotaxic space (Frauscher et al. 2018). The anatomical brain atlas was created with an unbiased method using data from 20 normal subjects and consisted of 132 gray matter labels (66 per hemisphere). Finally, each bipolar channel was represented by the volume of a cylinder of length equal to the distance between its two electrode contacts with 10-mm diameter, and the localization of each channel was determined to be the segmented region at which the majority of its volume was located.

iEEG signals were first band-pass filtered at 0.5–80 Hz and then downsampled to 200 Hz if the original sampling rate was higher (original sampling rates were 200, 256, 512, 1000, 1024, and 2000 Hz), line noise at 50 or 60 Hz (whichever was applicable) was removed, and time series from each electrode was Z-normalized by removing mean and scaling by the standard deviation. For filtering, including in the ultralow-delta frequency band (<4 Hz), we used a fourth-order two-way zero phase lag Butterworth filter throughout the analysis.

UPENN-RAM iEEG Cohort

iEEG recordings from 102 patients shared by Kahana and colleagues at the University of Pennsylvania (UPENN) (obtained from the UPENN-RAM public data release under release ID "Release_20171012," released on 12 October 2017) were used as the replication cohort (Jacobs et al. 2016). iEEG recordings were downloaded from a UPENN-RAM consortium hosted data sharing archive (UPENN-RAM. RAM—Computational Memory Lab. URL: http://memory.psych.upenn.edu/RAM). Prior to data collection, research protocols and ethical guidelines were approved by the Institutional Review Board at the participating hospitals, and informed consent was obtained from the participants and guardians (Jacobs et al. 2016). Details of all the recordings sessions and data preprocessing procedures are described by Kahana and colleagues (Jacobs et al. 2016). Briefly, iEEG recordings were obtained using subdural grids and strips (contacts placed 10 mm apart) or depth electrodes (contacts spaced 5–10 mm apart) using recording systems at each clinical site. iEEG systems included DeltaMed XlTek (Natus), Grass Telefactor, and Nihon-Kohden EEG systems. Electrodes located in brain lesions or those which corresponded to seizure onset zones or had significant interictal spikings or had broken leads were excluded from analysis. Resting-state data were extracted from patients performing multiple trials of a "free recall" experiment, where they were first presented with a list of words and later asked to recall as many as possible from the original list. We analyzed recordings during the intertrial intervals when subjects were given no explicit cognitive task thus presumably emulating "explicit resting-state" connectivity, similar to previous iEEG studies (Miller et al. 2009; Yanagisawa et al. 2012; Horak et al. 2017; Norman et al. 2017). Specifically, we extracted 10-s iEEG recordings (epochs) prior to the beginning of each trial. To reduce boundary and carry over effects, we discarded 3 s each of iEEG data from the beginning and end of each epoch, resulting in multiple 4-s epochs (Betzel et al. 2019). Data from each epoch was analyzed separately, and specific linear and nonlinear measures were averaged across trials. Even though each trial was ~4 s in duration, we had multiple trials for each subject. The average number of trials across all subjects was ~22. Hence, for each subject, we had ~88 s of recordings, which is in the order of the recordings from the MNI cohort (~60 s). These values are also typical based on previous iEEG studies (Miller et al. 2009; Yanagisawa et al. 2012; Horak et al. 2017; Norman et al. 2017).

Anatomical localization of electrode placement was accomplished by coregistering the postoperative computed CTs with the postoperative MRIs using FSL (FMRIB (Functional MRI of the Brain) Software Library), BET (Brain Extraction Tool), and FLIRT (FMRIB Linear Image Registration Tool) software packages. Preoperative MRIs were used when postoperative MRIs were not available. The resulting contact locations were mapped to MNI space using an indirect stereotactic technique and OsiriX Imaging Software DICOM viewer package. We used the Harvard–Oxford atlas (Frazier et al. 2005; Desikan et al. 2006; Goldstein et al. 2007) for mapping electrodes to ACC, PCC, precuneus, MFG, and SMG. We used the Deen atlas (Deen et al. 2011) to demarcate the AI.

iEEG signals were sampled at 1000 Hz. Signals recorded at individual electrodes were converted to a bipolar montage by computing the difference in signal between adjacent electrode pairs on each strip, grid, and depth electrode, and the resulting bipolar signals were treated as new virtual electrodes originating from the midpoint between each contact pair. Line noise (60 Hz) and its harmonics were removed from the bipolar signals, and finally each bipolar signal was Z-normalized by removing mean and scaling by the standard deviation. Similar to MNI analysis, for filtering, including in the ultralow-delta frequency band (<4 Hz), we used a fourth-order two-way zero phase lag Butterworth filter throughout the analysis.

Participant and Electrode Identification in the MNI and UPENN-RAM Cohorts

We first used the primary cohort (MNI) to identify electrodes in the AI and ACC nodes of the SN, PCC/precuneus nodes of the DMN, and MFG and SMG nodes of the FPN. We identified

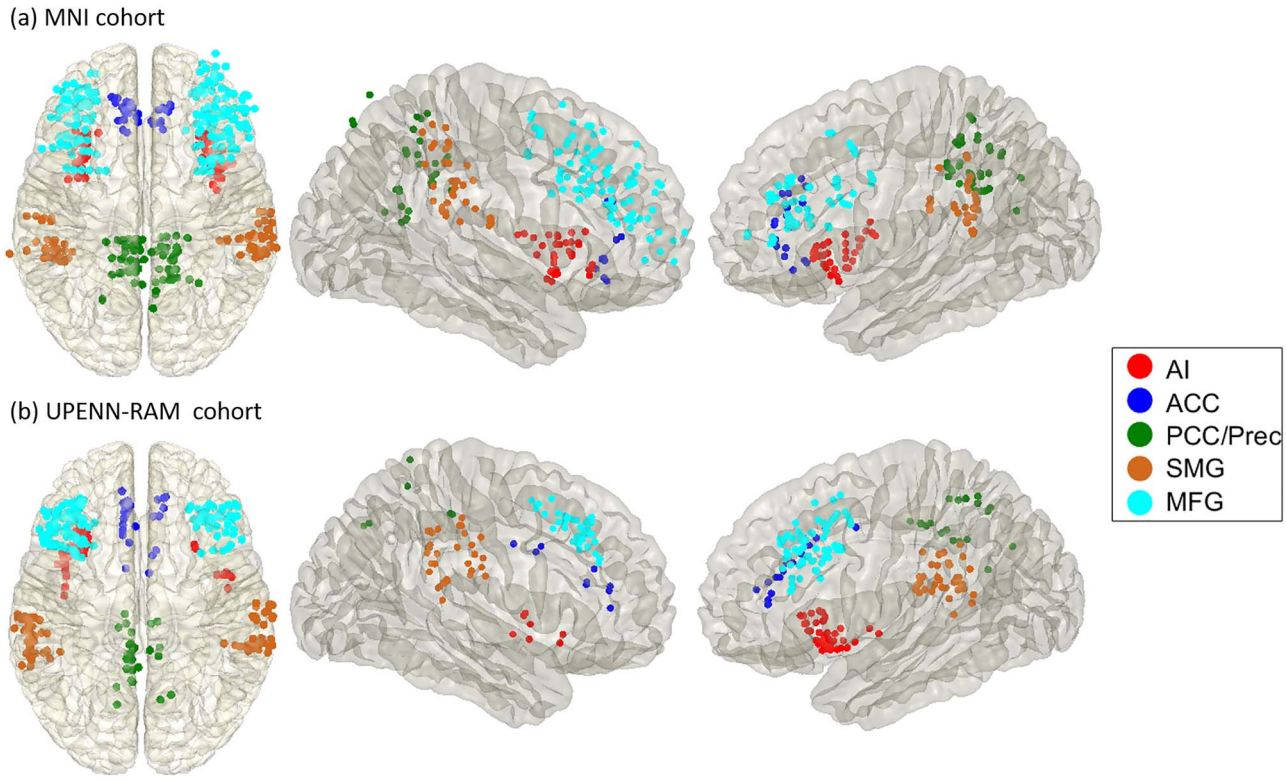

Figure 1. Salience network, default mode network and frontoparietal network iEEG recording sites in the primary (MNI) and replication (UPENN-RAM) cohorts. (*a*) MNI Cohort: iEEG recording sites in the salience network (SN), default mode network (DMN), and frontoparietal network (FPN). Electrodes in the anterior insula (AI, red), anterior cingulate cortex (ACC, blue) nodes of the SN, posterior cingulate cortex (PCC)/precuneus nodes of the DMN (green), and middle frontal gyrus (MFG, cyan) and supramarginal gyrus (SMG, brown) nodes of the FPN. (*b*) UPENN-RAM Cohort: iEEG recording sites. Analysis of iEEG data was first performed on the MNI cohort and replicability examined using the UPENN-RAM cohort.

electrode pairs in which there were at least five patients with electrodes implanted in two brain networks of interest (e.g., SN and DMN). Given our focus on the SN, we identified participants who had electrode pairs AI–ACC and SN–X, where X represents electrodes in the PCC/precuneus which constitute the posterior medial node of the DMN and the MFG and SMG nodes which constitute the FPN (Fig. 1*a*, Supplementary Tables 1, 2*a* and 3*a*; see also Supplementary Table 4*a* for participant demographics). The same procedures were used to identify participants and electrode pairs in the UPENN-RAM cohort, which was used as the replication dataset in our study (Fig. 1*b*, Supplementary Tables 2*b* and 3*b*; see also Supplementary Table 4*b* for participant demographics). Similar to the MNI cohort, we identified electrode pairs in which there were at least five patients with electrodes implanted in two brain networks of interest (e.g., SN and DMN), the only exception being the AI–ACC which had four patients with electrodes in both regions. In both cohorts, electrodes from left and right hemispheres of each brain region (e.g., SN) were pooled to increase the number of electrode pairs across which all subsequent analyses were performed.

iEEG Analysis: Linear and Nonlinear Measures

Correlation Analysis

Pearson correlation coefficient r between pairwise ROIs were computed as

$$r = \frac{\sum_{i=1}^{n} (x_i - \bar{x})(y_i - \bar{y})}{\sqrt{\sum_{i=1}^{n} (x_i - \bar{x})^2}\sqrt{\sum_{i=1}^{n} (y_i - \bar{y})^2}}, \quad (1)$$

where n is the number of time samples, $\{x_i\}$ and $\{y_i\}$ are the time series of the two ROIs of interest, and $\bar{x} = \frac{1}{n}\sum_{i=1}^{n} x_i$ and $\bar{y} = \frac{1}{n}\sum_{i=1}^{n} y_i$ are the sample means of time series $\{x_i\}$ and $\{y_i\}$, respectively.

PTE and Causal Analysis

A brain region has a causal influence on a target if knowing the past of both signals improves the ability to predict the target's future in comparison to knowing only the target's past (Granger 1969; Marinazzo et al. 2008). PTE is a nonlinear measure of the directionality of information flow between time series (Lobier et al. 2014). In contrast, Granger causality analysis (Barnett and Seth 2014) can estimate the directionality of only linear interactions. Moreover, PTE is also computationally less expensive than transfer entropy (TE) (Lobier et al. 2014). Given two time series $\{x_i\}$ and $\{y_i\}$, where $i = 1, 2, \ldots, M$, instantaneous phases were first extracted using the Hilbert transform. Let $\{x_i^p\}$ and $\{y_i^p\}$, where $i = 1, 2, \ldots, M$, denote the corresponding phase time series. If the uncertainty of the target signal $\{y_i^p\}$ at delay τ is quantified using Shannon entropy, then the PTE from driver signal $\{x_i^p\}$ to target signal $\{y_i^p\}$ can be given by

$$\mathrm{PTE}_{x\to y} = \sum_i p\left(y_{i+\tau}^p, y_i^p, x_i^p\right) \log\left(\frac{p\left(y_{i+\tau}^p | y_i^p, x_i^p\right)}{p\left(y_{i+\tau}^p | y_i^p\right)}\right), \quad (2)$$

where the probabilities can be calculated by building histograms of occurrences of singles, pairs, or triplets of instantaneous

phase estimates from the phase time series (Hillebrand et al. 2016). For our analysis, the number of bins in the histograms was set as $3.49 \times \mathrm{STD} \times M^{-1/3}$, and delay τ was set as $2M/M_{\pm}$, where STD is average standard deviation of the phase time series $\{x_i^p\}$ and $\{y_i^p\}$ and $M_{\pm}$ is the number of times the phase changes sign across time and channels (Hillebrand et al. 2016). Note that PTE is robust against the choice of the delay τ and the number of bins for forming the histograms and variations in these parameters do not change the results much (Hillebrand et al. 2016). For PTE estimation, we used the broadband signal (0.5–80 Hz) rather than filtering the signal in the delta band, since causality estimation is very sensitive to filtering (see Barnett and Seth 2011 for a detailed discussion on this).

Net causal outflow was calculated as the difference between the total outgoing information and total incoming information, that is, net causal outflow = PTE(out) – PTE(in). In both cohorts, for calculation of PTE(out) and PTE(in) for SN electrodes, electrodes in the DMN and FPN were considered, that is, PTE(out) was calculated as the net PTE from SN electrodes to the DMN and FPN electrodes, and PTE(in) was calculated as the net PTE from the DMN and FPN electrodes to SN electrodes. Similarly, SN and FPN electrodes were considered for calculation of net causal outflow of the DMN electrodes. For calculating net causal outflow of FPN, the SN and DMN electrodes were considered.

Decorrelation Time Analysis

For linear dependency, the first zero crossing of the autocorrelation function (Theiler 1986) of the time series of an electrode was considered as its memory. Nonlinear memory was estimated as the first local minimum of the mutual information (MI) function of the electrode time-series recordings (Fraser and Swinney 1986).

Multiscale Sample Entropy (MSE) Analysis

Multiscale sample entropy (MSE) is used to characterize the "complexity" of a time series by analyzing its nonlinear features (Richman and Moorman 2000). Given a time series $\{x_i\}$, where $i = 1, 2, \ldots, M$, we first construct consecutive coarse-grained time series $\{y_j^{(\xi)}\}$ with scale factor ξ. To do this, we divide time series $\{x_i\}$ into nonoverlapping windows of length ξ and then average the data points inside each window as

$$y_j^{(\xi)} = \frac{1}{\xi} \sum_{i=(j-1)\xi+1}^{j\xi} x_i, \quad 1 \le j \le M/\xi. \tag{3}$$

Note that for scale 1, time series $\{y_j^{(1)}\}$ is the same as the original time series and the length of each coarse-grained time series is equal to the length of the original time series divided by the scale factor ξ. Small ξ represents short-range temporal scale, and larger ξ values represent longer temporal scales. We next calculate the sample entropy for each coarse-grained time series. Given coarse-grained time series $\{y_j^{(\xi)}\}$, where $1 \le j \le M/\xi$, we first construct the time-delay embedding given by $\boldsymbol{u}_j^{(\xi,m)} = (y_j^{(\xi)}, y_{j+\tau}^{(\xi)}, \ldots, y_{j+(m-1)\tau}^{(\xi)})$, where $1 \le j \le M/\xi - m\ \tau$, m is the embedding dimension, and τ is the embedding delay. We next count the number of instances P_i for which $d[\boldsymbol{u}_i^{(\xi,m)}, \boldsymbol{u}_j^{(\xi,m)}] \le r$, $j \ne i$, where $d[\boldsymbol{u}_i^{(\xi,m)}, \boldsymbol{u}_j^{(\xi,m)}]$ is the distance between any two embedding vectors $\boldsymbol{u}_i^{(\xi,m)}$ and $\boldsymbol{u}_j^{(\xi,m)}$ using the maximum norm and r is the threshold. We then calculate the probability that any two embedding vectors are similar in dimension m as

$$B^{(\xi,m)}(r) = \frac{1}{(M/\xi - m\ \tau)\,(M/\xi - m\ \tau - 1)} \sum_{i=1}^{M/\xi - m\ \tau} P_i. \tag{4}$$

Similarly, we construct the time-delay embedding for dimension $m+1$ given by $\boldsymbol{u}_j^{(\xi,m+1)} = (y_j^{(\xi)}, y_{j+\tau}^{(\xi)}, \ldots, y_{j+m\tau}^{(\xi)})$, where $1 \le j \le M/\xi - m\ \tau$. We count the number of instances Q_i for which $d[\boldsymbol{u}_i^{(\xi,m+1)}, \boldsymbol{u}_j^{(\xi,m+1)}] \le r$, $j \ne i$ and then calculate the probability that any two embedding vectors are similar in dimension $m+1$ as

$$B^{(\xi,m+1)}(r) = \frac{1}{(M/\xi - m\ \tau)\,(M/\xi - m\ \tau - 1)} \sum_{i=1}^{M/\xi - m\ \tau} Q_i. \tag{5}$$

For a given threshold r, sample entropy is calculated as the negative of the natural logarithm of the conditional probability that two embedding vectors close to each other in dimension m will also be close to each other when the dimension is increased by one as

$$\mathrm{SE} = -\ln\left[\frac{B^{(\xi,m+1)}(r)}{B^{(\xi,m)}(r)}\right] \tag{6}$$

Values of m, τ, and r were taken to be 2, 1, and 0.2 times the standard deviation of the time series for our analysis, respectively, as suggested by Pincus (2001). For both cohorts, the values of ξ were taken to be 1–5. Higher values of ξ were not considered since the estimation of sample entropy might be unreliable (Lu et al. 2015).

Results

With the goal of presenting and highlighting reproducible results, only results replicated in both the MNI and UPENN-RAM cohorts are reported and discussed.

We first identified all electrode pairs in the MNI iEEG (Frauscher et al. 2018) dataset which contained data from at least five participants (Fig. 1*a*, Supplementary Tables 1, 2*a* and 3*a*). Given our focus on the SN, we first examined iEEG data from participants who had electrode pairs AI–ACC in the SN and pairs SN–DMN and SN–FPN which reflect SN interactions with the DMN and FPN, respectively (Fig. 1*a*). There was insufficient coverage of electrode pairs spanning the SN and the ventromedial prefrontal cortex region of the DMN, so analyses of DMN electrodes were based on the PCC/precuneus. Analyses of the FPN electrodes were based on MFG and SMG regions. iEEG data analyses were first performed on the primary MNI cohort, and the same procedures were repeated in the replication UPENN-RAM cohort (Fig. 1*b*, Supplementary Tables 2*b* and 3*b*) (Jacobs et al. 2016). Demographic information for the participants of the MNI and UPENN-RAM iEEG datasets are shown in Supplementary Table 4*a*,*b*, respectively. Given the low-frequency nature of the fMRI signal and previous reports, based on simultaneous multisite electrophysiological and fMRI recordings in animal models which have demonstrated a strong correlation between synchronized ultralow-delta (<4 Hz) oscillations and resting-state fMRI signals (Lu et al. 2007; Chan et al. 2015; Jaime et al. 2019), we focused our analysis on the ultralow-delta (<4 Hz) band (hereafter referred to as slow-wave band (Dalal et al. 2011)). The length of each trial was ~4 s (see Materials and Methods) in the UPENN-RAM cohort which did

not allow us to analyze the ultralow band (<0.5 Hz) separately. We therefore combined ultralow and delta (0.5–4 Hz) frequency bands into a single ultralow-delta (<4 Hz) frequency band, and all analysis in our paper was carried out in this ultralow-delta frequency band across cohorts. Secondary analyses in the theta (4–8 Hz), alpha (8–12 Hz), beta (12–30 Hz), and gamma (30–80 Hz) bands did not reveal any systematic network signatures and are not discussed further. Our analysis pipeline, summarizing the linear and nonlinear measures used in this study, is shown in Figure 2.

Intra-SN Correlation Is Stronger than SN Interaction with DMN and FPN Electrodes

We first used linear correlation analysis to examine SN integrity and distinctiveness with respect to the DMN and FPN. In the MNI cohort, we found that intra-SN correlation in the slow-wave band was stronger than SN correlation with the DMN ($P < 0.05$) and FPN ($P < 0.05$) electrodes (Fig. 3*a*). Similarly, in the UPENN-RAM cohort, intra-SN correlation was stronger than SN correlation with the DMN ($P < 0.01$) and FPN ($P < 0.01$) electrodes (Fig. 3*b*). This result provides electrophysiological evidence that the AI and ACC are more strongly coupled with each other than with the DMN and FPN. Moreover, in both cohorts, intra-SN temporal correlation was also stronger than DMN–FPN correlation ($P < 0.01$ in MNI cohort and $P < 0.05$ in UPENN-RAM cohort) suggesting that intra-SN correlation is the strongest among all pairs of electrodes spanning the SN, DMN, and FPN.

No Evidence for Negative Correlations between SN and DMN

The question of whether the SN, or FPN, is intrinsically negatively correlated with the DMN has remained a controversy in fMRI research (Murphy et al. 2009) and one that ultimately needs resolution using electrophysiological recordings. We did not find any consistent evidence for long-time negative correlation in iEEG recordings between the SN, or FPN, and DMN electrodes in either the MNI or the UPENN-RAM cohort (Fig. 3).

SN Is a Causal Outflow Hub in Cross-Network Interactions with DMN and FPN

Previous fMRI studies have suggested that the SN acts as a causal outflow hub with respect to interactions with the DMN and FPN (Sridharan et al. 2008). To test the potential neural basis of this finding, we used PTE which provides a robust estimation of directed information flow between electrodes (see Materials and Methods for details). Net causal outflow was calculated as the difference between the total outgoing information and total incoming information (PTE(out)–PTE(in), see Materials and Methods for details). In this case, we used unfiltered time series since causality estimation is known to be sensitive to filtering (Barnett and Seth 2011). In both the MNI (Fig. 4*a*) and UPENN-RAM (Fig. 4*b*) cohorts, the SN had significantly higher net causal outflow than the DMN ($P < 0.001$ in both cohorts) and FPN ($P < 0.001$ and $P < 0.01$ in MNI and UPENN-RAM cohorts, respectively) electrodes. We did not find consistent differences between causal influences of the AI and ACC (Supplementary Figs 1 and 2).

These results demonstrate strong and replicable causal influences of the SN on the DMN and FPN and provide novel validation of dynamic causal influences that had previously been detected with fMRI data.

Shorter Decorrelation Times in SN, Compared to DMN and FPN Electrodes

The previous sections focused on interelectrode interactions related to SN integrity. In this and the following sections, we turn our attention to dynamic temporal features associated with SN time series. To test the hypothesis that the underlying temporal structure of SN time series differs from those of electrodes in the DMN and FPN, we examined long-range dependency of time series within each electrode. Temporal dependency was evaluated by computing the decorrelation time using both linear and nonlinear methods. In both cohorts, linear analysis revealed shorter decorrelation times in the SN electrodes compared to the FPN electrodes ($P < 0.05$ and $P < 0.001$ in MNI and UPENN-RAM cohorts, respectively) (Fig. 5). Nonlinear analyses revealed shorter decorrelation times in SN electrodes, compared to DMN ($P < 0.01$ and $P < 0.05$ in MNI and UPENN-RAM cohorts, respectively) and FPN ($P < 0.001$ in both cohorts) electrodes (Fig. 5). These results demonstrate faster temporal dynamics in the SN network and their replicability.

Higher Entropy of iEEG Activity in SN, Compared to DMN and FPN Electrodes

To further characterize the distinct nonlinear properties of the SN, we examined sample entropy (SE), which quantifies the "complexity" of a time series from its nonlinear features. We calculated SE from the original time series by constructing consecutive coarse-grained time series at multiple scales (see Materials and Methods for details) and then computing SE for each of these time series.

In the MNI cohort, for our primary analysis involving the original times series (scale 1), we found that SN electrodes had significantly higher SE, compared to DMN ($P < 0.01$) and FPN ($P < 0.001$) electrodes (Fig. 6*a*). Similarly, in the UPENN-RAM, the SN electrodes had significantly higher SE, compared to DMN ($P < 0.05$) and FPN ($P < 0.001$) electrodes (Fig. 6*b*).

We extended our analysis of sample entropy to multiple scales (five scales in both cohorts) and found similar results: in the MNI iEEG dataset, SN electrodes had significantly higher SE than the DMN electrodes for all other scales considered ($P < 0.01$ for scales 2–5) (Fig. 6*a*). SN electrodes also had significantly higher SE than the FPN electrodes at all other scales ($P < 0.001$ for scales 2–5) (Fig. 6*a*). Similarly, in the UPENN-RAM iEEG dataset, SN electrodes had significantly higher SE than the DMN electrodes for all other scales considered ($P < 0.05$ for scales 2–5) (Fig. 6*b*). SN electrodes also had significantly higher SE than the FPN electrodes at all other scales ($P < 0.001$ for scales 2–5) (Fig. 6*b*). These replicable results indicate greater entropy of iEEG signals in the SN, reflecting higher mean rate of creation of information at multiple time scales (Grassberger 1991; Costa et al. 2005).

Discussion

The SN is a large-scale distributed brain network anchored in the AI and ACC that plays a critical role in a wide range of

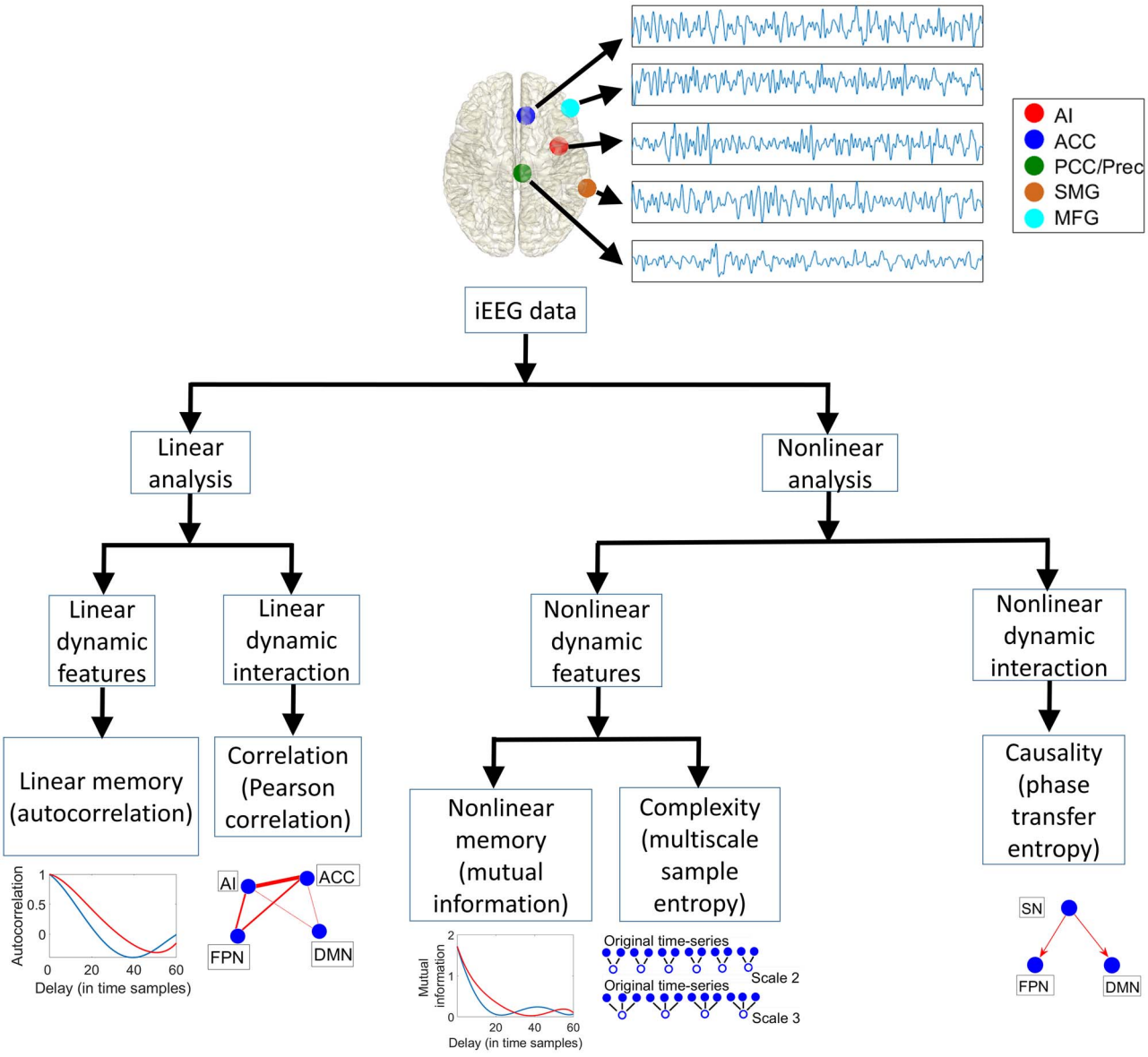

Figure 2. iEEG data analysis pipeline. Data analysis steps used to investigate differential intra- and cross-network connectivity of the SN electrodes, with DMN and FPN electrodes.

adaptive human behaviors (Dosenbach et al. 2006, 2008; Menon and Uddin 2010; Menon 2015a, 2015b). We used two independent iEEG cohorts to investigate the neurophysiological foundations of the SN and its dynamic interactions with the DMN and FPN. Critically, given the nonlinear nature of iEEG signals (Menon et al. 1996) and emerging findings of time-varying connectivity observed in fMRI data (Chen et al. 2016), both linear and nonlinear measures were used to probe the temporal dynamics of intra- and cross-network interactions that underpin the SN. Linear correlation revealed that intra-SN coupling is stronger than SN coupling with electrodes in the DMN and FPN. Dynamic causal analysis revealed the SN as a hub with respect to cross-network interactions with the DMN and FPN electrodes, underlying its role in fast temporal switching of networks (Sridharan et al. 2008). Further electrophysiological evidence for distinctiveness of the SN came from the analysis of temporal structure in regional electrophysiological activity within each electrode. Linear and nonlinear time series analysis both indicated faster temporal dynamics of activity in AI and ACC, compared to DMN and FPN nodes. Our findings provide new insights into SN integrity and the unique dynamic temporal properties that distinguish it from the DMN and FPN. Notably, all key results in the MNI cohort were replicated in the independent UPENN-RAM cohort, highlighting the robustness of our findings.

iEEG Temporal Correlations Reveal Neural Basis of SN Integrity

Distinct yet dynamically interacting large-scale functional networks that comprise the human brain have most readily and consistently been identified using fMRI (Menon 2015a,

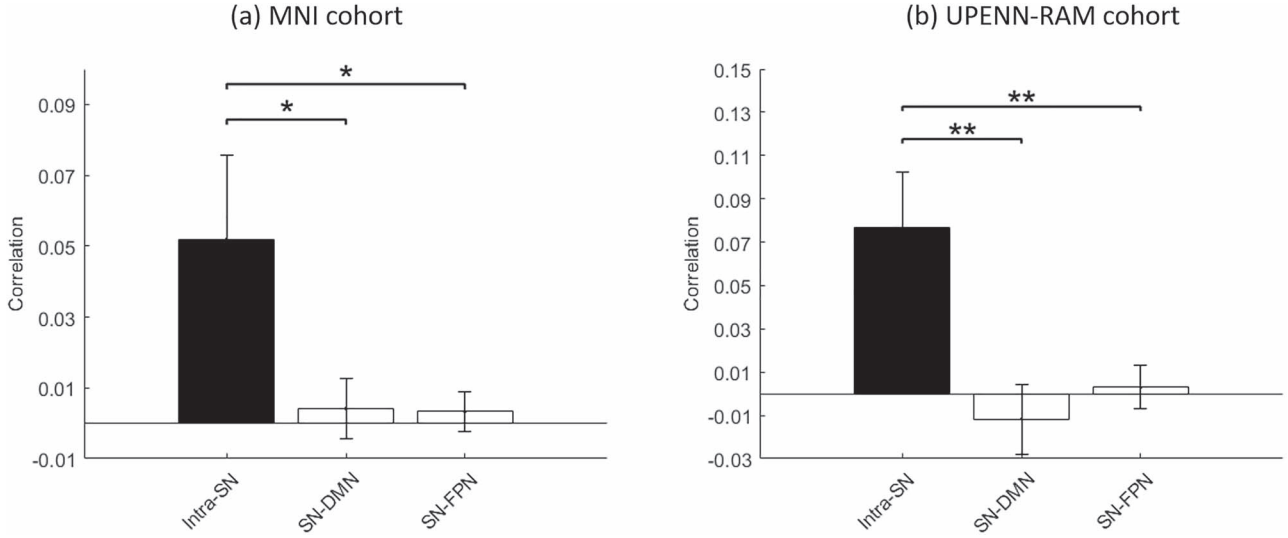

Figure 3. Intra-SN correlation of iEEG activity compared to SN correlation with DMN and FPN electrodes. (*a*) MNI cohort. (*b*) UPENN-RAM cohort. In both cohorts, intra-SN correlation was stronger compared to the correlation of the SN with the DMN and FPN electrodes. Error bars denote standard error of the mean (SEM) across all pairs of electrodes. $^{**}P < 0.01$, $^{*}P < 0.05$ (Mann–Whitney *U*-test).

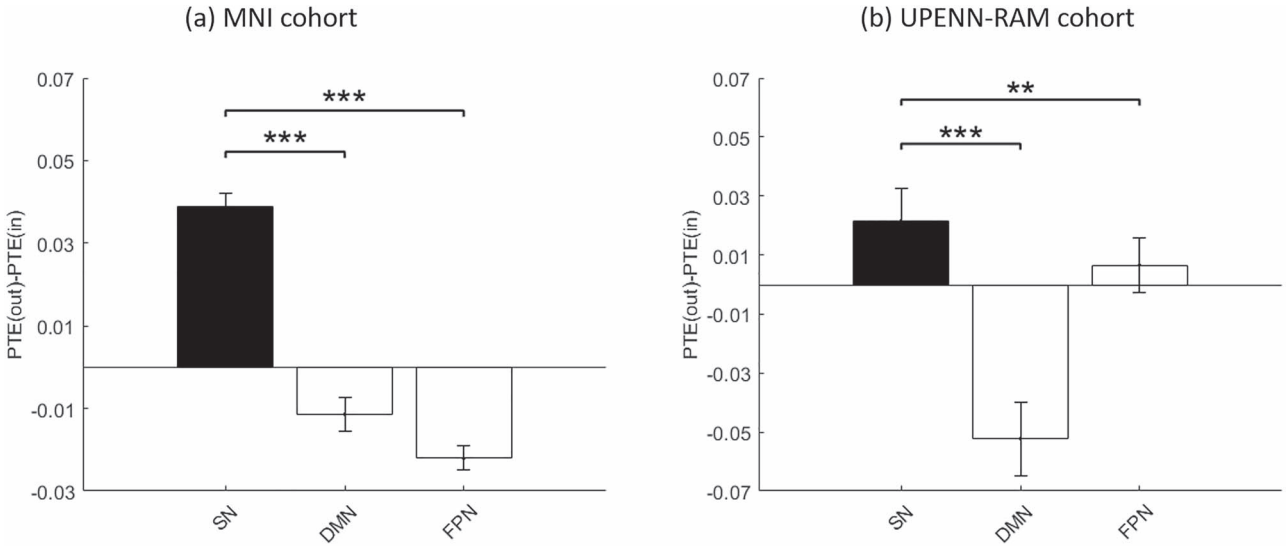

Figure 4. Net causal outflow of SN electrodes, compared to DMN and FPN electrodes. (*a*) MNI cohort. (*b*) UPENN-RAM cohort. Causality was estimated using PTE which characterizes directionality of nonlinear interactions between brain regions. Net causal outflow was calculated as the difference between the total outgoing information and total incoming information (PTE(out)–PTE(in)). In both cohorts, SN electrodes showed higher net causal outflow, when compared to the DMN and FPN electrodes. Error bars denote standard error of the mean (SEM) across all pairs of electrodes. $^{***}P < 0.001$, $^{**}P < 0.01$ (Mann–Whitney *U*-test).

2015b). Previous fMRI-based studies using both independent component analysis and seed-based connectivity analysis have consistently identified the SN as a fronto-opercular–cingulate network distinct from the DMN and FPN (Seeley et al. 2007). Our analysis of iEEG data revealed stronger intranetwork coupling in SN than cross-network coupling of SN with DMN and FPN electrodes. The intra-SN correlation was also the strongest among all pairs of electrodes spanning the SN, DMN, and FPN. Spectral analysis revealed that the strongest and most consistent effects were in the slow-wave frequency band (<4 Hz), consistent with observations in human EEG and MEG recordings (Schroeder and Lakatos 2009; Hirvonen et al. 2018) as well as animal local field potential (LFP) recordings (Jaime et al. 2019). These findings provide novel electrophysiological evidence for the integrity and distinctiveness of the SN.

Weak and Inconsistent Evidence for Negative Correlations between SN and DMN in Resting-State iEEG

The lack of negative correlation between the SN, or FPN, and the DMN electrodes is consistent with reports based on task-free local field potential recordings in a cat visual cortex (Popa et al. 2009). Our findings suggest that negative correlations of the SN, or FPN, with the DMN may arise mainly from dynamic changes in activation and deactivation that occur

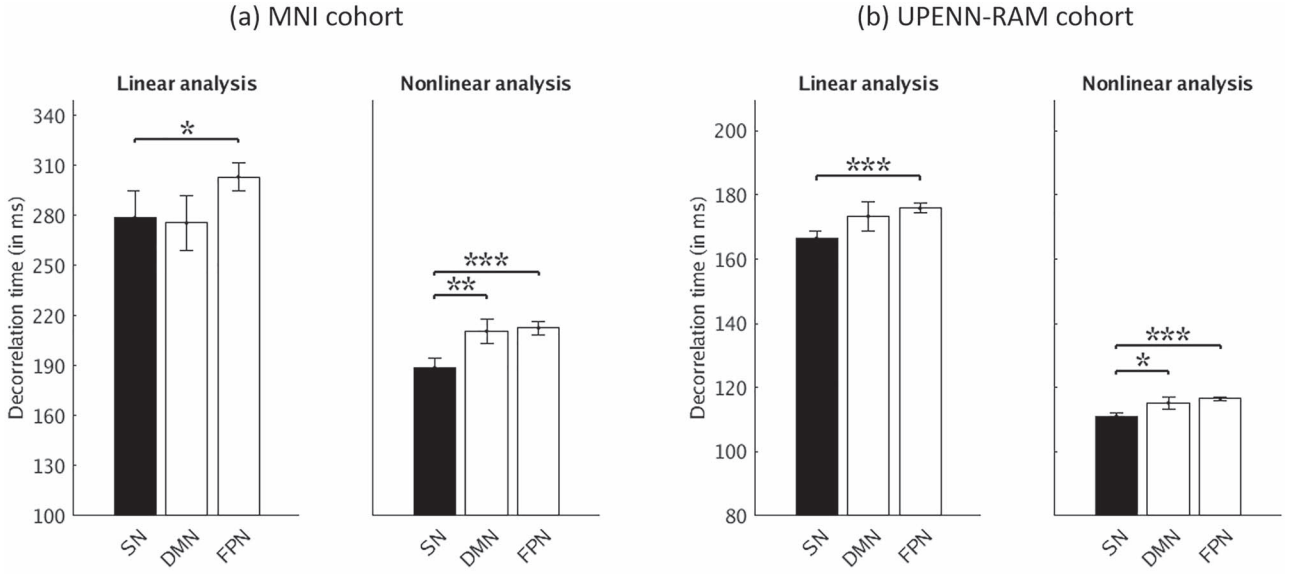

Figure 5. Decorrelation times of iEEG activity in SN, compared to DMN and FPN electrodes using both linear and nonlinear analysis. (*a*) MNI cohort. (*b*) UPENN-RAM cohort. Decorrelation time, the interval in which past "memory" in the time series is lost, was determined using both linear and nonlinear measures. In linear analysis, SN electrodes had shorter decorrelation times in comparison to the FPN electrodes in both cohorts. In nonlinear analysis, SN electrodes had shorter decorrelation times in comparison to the DMN and FPN electrodes in both cohorts. Error bars denote standard error of the mean (SEM) across all electrodes. $^{***}P < 0.001$, $^{**}P < 0.01$, $^{*}P < 0.05$ (Mann–Whitney *U*-test).

during cognition, rather than being an intrinsic feature of their functional organization (Greicius and Menon 2004). Further research with resting-state and task-based slow-wave frequency iEEG recordings is needed to probe the neurophysiological basis of putative anticorrelated interactions across large-scale brain networks.

Causal Dynamics and Hubs in the SN

Previous fMRI studies have suggested that SN plays an important role in its task-related engagement and disengagement of the DMN across a wide range of cognitive and affective tasks (Chen et al. 2016). These studies have shown that SN nodes have earlier latency and exert stronger causal influences to DMN and FPN nodes during cognition. Higher causal influences of the AI node of the SN on multiple brain areas have also been reported in resting-state fMRI (Deshpande et al. 2011; Zhou et al. 2018). Despite the consistency of these findings across task-related and resting-state fMRI studies, it is not clear whether these observations have a neuronal basis or whether they are an artifactual feature of fMRI signals arising from its slow dynamics and regional variation in hemodynamic response function.

To address this question, we used PTE, which provides a robust and powerful tool for characterizing information flow between brain regions based on phase coupling (Lobier et al. 2014; Hillebrand et al. 2016; Wang et al. 2017). Analogous to the formulation in Granger causal analysis, a brain region has a stronger causal influence on a target if knowing the past phase of signals in both regions improves the ability to predict the target's phase in comparison to knowing only the target's past phase (Granger 1969). However, PTE has several advantages over Granger causal analysis (Barnett and Seth 2011), as it 1) can capture nonlinear interactions, 2) is more accurate and computationally less expensive than transfer entropy, and 3) estimates causal interactions based on phase, rather than amplitude, coupling (Schreiber 2000; Lobier et al. 2014; Hillebrand et al. 2016).

PTE revealed significantly higher net causal outflow in SN electrodes than DMN and FPN electrodes, in both MNI and UPENN-RAM cohorts. To evaluate the overall temporal pattern of causal interactions, we computed a causal hub metric based on difference between PTE for out versus in links. We found that the SN had stronger causal influences on DMN and FPN electrodes, thus providing novel electrophysiological evidence for their role as a causal signaling hub. This pattern of neuronal signaling may underlie the SN's causal role in facilitating dynamic switching between the DMN and FPN. Our findings thus provide novel electrophysiological evidence that the SN plays a prominent causal role in signaling with other brain networks (Sridharan et al. 2008; Cai et al. 2016) and is consistent with the temporal order of task-evoked responses reported using cortical electrogram recordings (Raccah et al. 2018). We suggest that the SN's causal influences on the DMN and FPN give it a powerful and flexible role in cognitive control as hypothesized previously based on fMRI studies (Dosenbach et al. 2008; Menon and Uddin 2010; Chen et al. 2016). Further research with both task and resting-state iEEG data and dense sampling of electrodes in multiple cortical and subcortical regions, as well as the AI and ACC, are necessary to further probe the broader causal role of the SN in the human brain.

Fast Temporal Dynamics of iEEG Activity in the SN

The AI and ACC nodes of the SN were further distinguished by their intrinsic dynamic properties. Decorrelation time and sample entropy have been extensively used in the neuroscience literature to probe neural dynamics and have been shown to play important roles in cognition (Sokunbi et al. 2013; Wang et al. 2014, 2018; Cavanagh et al. 2016; Jia et al. 2017; Pedersen et al. 2018; Saxe et al. 2018; Wairagkar et al. 2018; Xue et al. 2019).

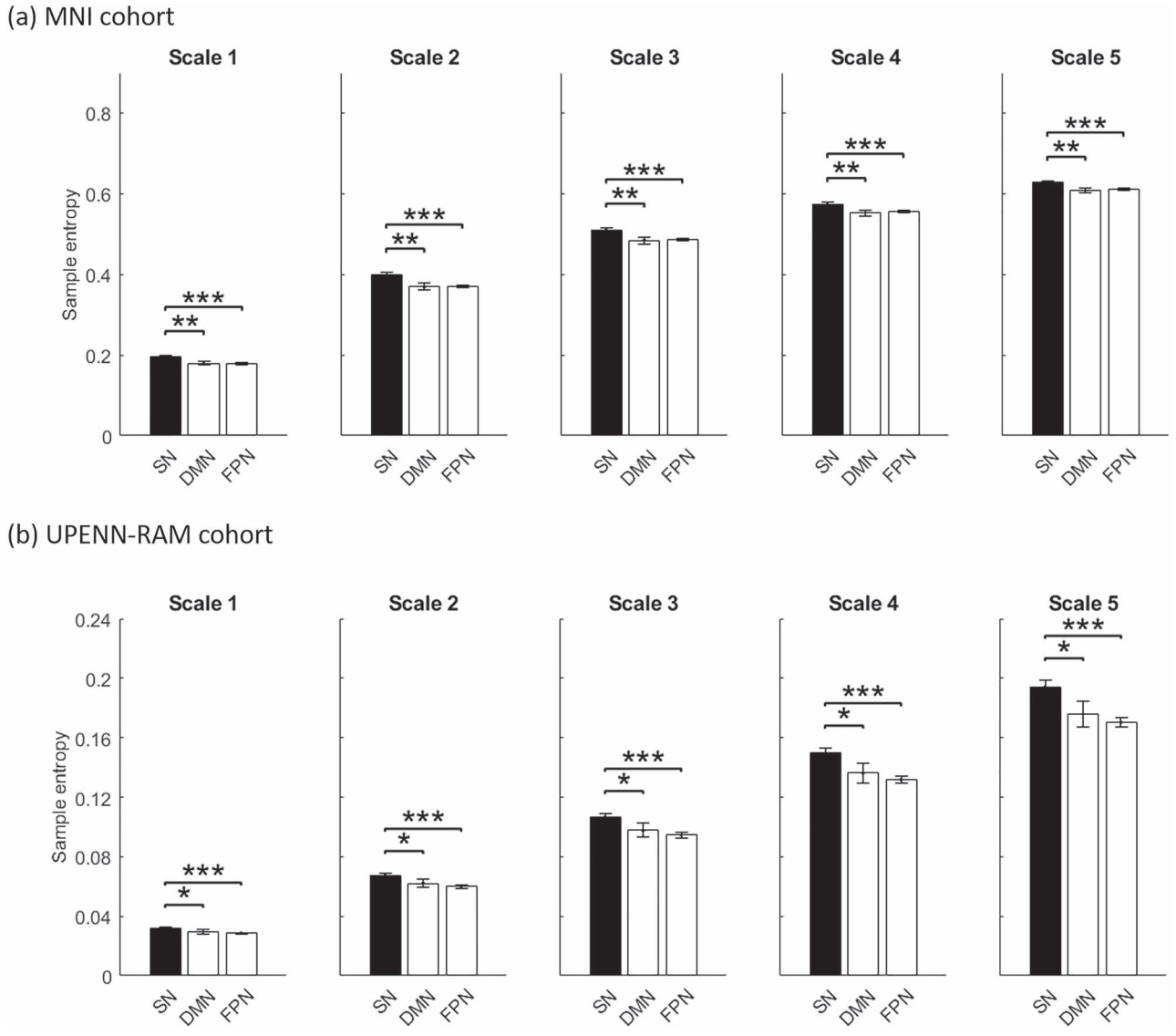

Figure 6. Entropy of iEEG activity in SN electrodes, compared to DMN and FPN electrodes. (*a*) MNI cohort. (*b*) UPENN-RAM cohort. Sample entropy (SE) was used to quantify the rate of information creation from its nonlinear dynamical features. In both cohorts, SN electrodes had higher entropy in comparison to the DMN and FPN electrodes. Error bars denote standard error of the mean (SEM) across all electrodes. $^{***}P < 0.001$, $^{**}P < 0.01$, $^{*}P < 0.05$ (Mann–Whitney *U*-test).

For example, it has been shown that decorrelation time can distinguish between resting-state and movement intention and can play an important role in designing better brain–computer interfaces (Wairagkar et al. 2018). Furthermore, variability of decorrelation time across neurons in the prefrontal cortex predicts involvement in decision-making processes (Cavanagh et al. 2016).

Linear autocorrelation-based analysis revealed shorter decorrelation times in SN electrodes compared to FPN electrodes and comparable decorrelation times in SN electrodes compared to DMN electrodes. Nonlinear mutual information-based analysis revealed shorter decorrelation times in SN electrodes, in comparison to DMN and FPN electrodes. This highlights the importance of taking nonlinear features into account in analyzing neuronal dynamics and suggests that distinguished features between two brain networks can be missed by linear analysis only.

Decorrelation times capture the interval in which past "memory" in the time series is lost, and our finding of faster decorrelation times in SN is consistent with its hypothesized role in facilitating fast temporal interactions with other brain networks (Dosenbach et al. 2006, 2008; Sridharan et al. 2008; Chen et al. 2016). Multiscale entropy measures which assess complexity and information in dynamical systems (Grassberger 1991) revealed higher entropy in the SN, which further distinguished SN activity from the DMN and FPN. Thus, multiple quantitative approaches provide converging evidence for fast temporal features associated with the AI and ACC. These unique dynamic temporal properties of the SN may underlie its flexible role in initiating network switching and mediating

causal interactions between brain networks (Sridharan et al. 2008; Bressler and Menon 2010; Menon 2011; Taghia et al. 2018).

SN Stability and Flexibility

Our linear correlation and nonlinear causal analyses identify distinct temporal features associated with network stability and flexibility. On the one hand, we found that intranetwork correlation of the SN was significantly higher than cross-network correlations with the DMN and FPN. On the other hand, causal analyses, which capture temporal delay-dependent dynamics, uncovered the influence of the SN on the DMN and FPN. Together, these neurophysiological properties may allow the SN to maintain a balance between network stability and flexibility. Critically, linear analysis captures network stability, while nonlinear analysis captures flexibility. In terms of cognitive function, our findings indicate that SN nodes have the intrinsic capacity to influence other brain networks which may help facilitate dynamic state changes associated with both internal mental events and the external environment. Further iEEG studies comparing task-related and stimulus-related responses are required to test this hypothesis.

Reproducibility of Findings

Reproducibility is a challenge for all of neuroscience but particularly so for invasive human intracranial electrophysiological studies where data is hard to obtain and open-source data sharing is rare (Jacobs et al. 2016; Frauscher et al. 2018). To address this concern and to determine the reliability of our findings, we used two unique iEEG datasets shared by the MNI (Frauscher et al. 2018) and UPENN-RAM (Jacobs et al. 2016) consortia. Despite differences in acquisition sites, recording systems, and protocols, we replicated three major results across the two cohorts: 1) SN nodes showed stronger correlation with each other, when compared to the DMN and FPN, 2) the SN is a dynamic causal hub in relation to its interaction with the DMN and FPN, and 3) the SN showed faster temporal dynamics and higher entropy than electrodes in the DMN and FPN. These results provide robust evidence for the unique electrophysiological properties of the SN and its dynamic temporal properties.

Conclusion

Our study significantly advances knowledge of the neurophysiological underpinnings of large-scale networks in the human brain. Convergent evidence from multiple quantitative measures revealed a unique profile of intra- and cross-network interactions, and dynamic temporal properties, that characterize the SN and distinguish it from other brain networks. Analysis of linear dynamical properties revealed higher levels of correlated activity between the AI and ACC nodes of the SN than with regions belonging to the other networks. SN nodes showed unique causal relationships with the other brain regions and also have different intrinsic signal dynamics. More broadly, our findings provide new insights and perspectives into foundational mechanisms underlying stability and flexibility of large-scale networks in the human brain. Finally, our study demonstrates how iEEG data sharing efforts can facilitate reproducibility and help propel discoveries in human system neuroscience that would be otherwise virtually impossible to achieve (Holdgraf et al. 2019).

Supplementary Material

Supplementary material can be found at *Cerebral Cortex* online.

Funding

NIH (grants NS086085, EB022907).

Notes

We are grateful to members of the MNI and UPENN-RAM consorts for generously sharing their precious iEEG data. We thank Drs. Birgit Frauscher and Nicolas Von Ellenrieder for the assistance with the MNI dataset and Drs Paul A. Wanda, Michael V. DePalatis, Youssef Ezzyat, Richard Betzel, and Leon A. Davis for the assistance with the UPENN-RAM dataset. We thank Drs Matteo Fraschini and Arjan Hillebrand for generously sharing their MATLAB code for phase transfer entropy analysis. We also thank Dr Weidong Cai for helping with the Harvard–Oxford and Deen atlases, Dr Aarthi Padmanabhan for her valuable feedback on the manuscript, and Christopher Hamblin for helping with parallelizing data analysis. *Conflict of Interest*: None declared.

References

Barnett L, Seth AK. 2011. Behaviour of granger causality under filtering: theoretical invariance and practical application. *J Neurosci Methods*. 201:404–419.

Barnett L, Seth AK. 2014. The MVGC multivariate granger causality toolbox: a new approach to Granger-causal inference. *J Neurosci Methods*. 223:50–68.

Betzel RF, Medaglia JD, Kahn AE, Soffer J, Schonhaut DR, Bassett DS. 2019. Structural, geometric and genetic factors predict interregional brain connectivity patterns probed by electrocorticography. *Nat Biomed Eng*. 3:902–916.

Bressler SL, Menon V. 2010. Large-scale brain networks in cognition: emerging methods and principles. *Trends Cogn Sci*. 14:277–290.

Cai W, Chen T, Ryali S, Kochalka J, Li CS, Menon V. 2016. Causal interactions within a frontal-cingulate-parietal network during cognitive control: convergent evidence from a multisite-multitask investigation. *Cereb Cortex*. 26:2140–2153.

Cai W, Ryali S, Chen T, Li CS, Menon V. 2014. Dissociable roles of right inferior frontal cortex and anterior insula in inhibitory control: evidence from intrinsic and task-related functional parcellation, connectivity, and response profile analyses across multiple datasets. *J Neurosci*. 34:14652–14667.

Cavanagh SE, Wallis JD, Kennerley SW, Hunt LT. 2016. Autocorrelation structure at rest predicts value correlates of single neurons during reward-guided choice. *elife*. 5:pii:e18937.

Chan AW, Mohajerani MH, LeDue JM, Wang YT, Murphy TH. 2015. Mesoscale infraslow spontaneous membrane potential fluctuations recapitulate high-frequency activity cortical motifs. *Nat Commun*. 6:7738.

Chen T, Cai W, Ryali S, Supekar K, Menon V. 2016. Distinct global brain dynamics and spatiotemporal organization of the salience network. *PLoS Biol*. 14:e1002469.

Costa M, Goldberger AL, Peng CK. 2005. Multiscale entropy analysis of biological signals. *Phys Rev E*. 71:021906.

Dalal SS, Vidal JR, Hamame CM, Ossandon T, Bertrand O, Lachaux JP, Jerbi K. 2011. Spanning the rich spectrum of the human brain: slow waves to gamma and beyond. *Brain Struct Funct*. 216:77–84.

Dastjerdi M, Foster BL, Nasrullah S, Rauschecker AM, Dougherty RF, Townsend JD, Chang C, Greicius MD, Menon V, Kennedy DP *et al*. 2011. Differential electrophysiological response during rest, self-referential, and non–self-referential tasks in human posteromedial cortex. *PNAS*. 108:3023–3028.

Deen B, Pitskel NB, Pelphrey KA. 2011. Three systems of insular functional connectivity identified with cluster analysis. *Cereb Cortex*. 21:1498–1506.

Deshpande G, Santhanam P, Hu X. 2011. Instantaneous and causal connectivity in resting state brain networks derived from functional MRI data. *NeuroImage*. 54:1043–1052.

Desikan RS, Ségonne F, Fischl B, Quinn BT, Dickerson BC, Blacker D, Buckner RL, Dale AM, Maguire RP, Hyman BT *et al*. 2006. An automated labeling system for subdividing the human cerebral cortex on MRI scans into gyral based regions of interest. *NeuroImage*. 31:968–980.

Dosenbach NU, Fair DA, Cohen AL, Schlaggar BL, Petersen SE. 2008. A dual-networks architecture of top-down control. *Trends Cogn Sci*. 12:99–105.

Dosenbach NU, Visscher KM, Palmer ED, Miezin FM, Wenger KK, Kang HC, Burgund ED, Grimes AL, Schlaggar BL, Petersen SE. 2006. A core system for the implementation of task sets. *Neuron*. 50:799–812.

Fraser AM, Swinney HL. 1986. Independent coordinates for strange attractors from mutual information. *Phys Rev A*. 33:1134–1140.

Frauscher B, von Ellenrieder N, Zelmann R, Doležalová I, Minotti L, Olivier A, Hall J, Hoffmann D, Nguyen DK, Kahane P *et al*. 2018. Atlas of the normal intracranial electroencephalogram: neurophysiological awake activity in different cortical areas. *Brain*. 141:1130–1144.

Frazier JA, Chiu S, Breeze JL, Makris N, Lange N, Kennedy DN, Herbert MR, Bent EK, Koneru VK, Dieterich ME *et al*. 2005. Structural brain magnetic resonance imaging of limbic and thalamic volumes in pediatric bipolar disorder. *AJP*. 162:1256–1265.

Freeman W. 2000. *Neurodynamics: an exploration in mesoscopic brain dynamics*. London: Springer-Verlag.

Goldstein JM, Seidman LJ, Makris N, Ahern T, O'Brien LM, Caviness VS, Kennedy DN, Faraone SV, Tsuang MT. 2007. Hypothalamic abnormalities in schizophrenia: sex effects and genetic vulnerability. *Biol Psychiatry*. 61:935–945.

Granger CWJ. 1969. Investigating causal relations by econometric models and cross-spectral methods. *Econometrica*. 37:424–438.

Grassberger P. 1991. Information and complexity measures in dynamical systems. In: Atmanspacher H, Scheingraber H, editors. *Information dynamics*. Boston, MA: Springer US, pp. 15–33.

Greicius MD, Kiviniemi V, Tervonen O, Vainionpää V, Alahuhta S, Reiss AL, Menon V. 2008. Persistent default-mode network connectivity during light sedation. *Hum Brain Mapp*. 29:839–847.

Greicius MD, Menon V. 2004. Default-mode activity during a passive sensory task: uncoupled from deactivation but impacting activation. *J Cogn Neurosci*. 16:1484–1492.

Hillebrand A, Tewarie P, Dellen EV, Yu M, Carbo EWS, Douw L, Gouw AA, Straaten ECWV, Stam CJ. 2016. Direction of information flow in large-scale resting-state networks is frequency-dependent. *Proc Natl Acad Sci U S A*. 113: 3867–3872.

Hirvonen J, Monto S, Wang SH, Palva JM, Palva S. 2018. Dynamic large-scale network synchronization from perception to action. *Neural Netw*. 2:442–463.

Holdgraf C, Appelhoff S, Bickel S, Bouchard K, D'Ambrosio S, David O, Devinsky O, Dichter B, Flinker A, Foster BL *et al*. 2019. iEEG-BIDS, extending the brain imaging data structure specification to human intracranial electrophysiology. *Sci Data*. 6:102.

Horak PC, Meisenhelter S, Song Y, Testorf ME, Kahana MJ, Viles WD, Bujarski KA, Connolly AC, Robbins AA, Sperling MR *et al*. 2017. Interictal epileptiform discharges impair word recall in multiple brain areas. *Epilepsia*. 58:373–380.

Jacobs J, Miller J, Lee SA, Coffey T, Watrous AJ, Sperling MR, Sharan A, Worrell G, Berry B, Lega B *et al*. 2016. Direct electrical stimulation of the human entorhinal region and hippocampus impairs memory. *Neuron*. 92:983–990.

Jaime S, Gu H, Sadacca BF, Stein EA, Cavazos JE, Yang Y, Lu H. 2019. Delta rhythm orchestrates the neural activity underlying the resting state BOLD signal via phase–amplitude coupling. *Cereb Cortex*. 29:119–133.

Jia Y, Gu H, Luo Q. 2017. Sample entropy reveals an age-related reduction in the complexity of dynamic brain. *Sci Rep*. 7:7990.

Jilka SR, Scott G, Ham T, Pickering A, Bonnelle V, Braga RM, Leech R, Sharp DJ. 2014. Damage to the salience network and interactions with the default mode network. *J Neurosci*. 34:10798–10807.

Kucyi A, Schrouff J, Bickel S, Foster BL, Shine JM, Parvizi J. 2018. Intracranial electrophysiology reveals reproducible intrinsic functional connectivity within human brain networks. *J Neurosci*. 38:4230–4242.

Lobier M, Siebenhühner F, Palva S, Palva JM. 2014. Phase transfer entropy: a novel phase-based measure for directed connectivity in networks coupled by oscillatory interactions. *NeuroImage*. 85:853–872.

Lu H, Zuo Y, Gu H, Waltz JA, Zhan W, Scholl CA, Rea W, Yang Y, Stein EA. 2007. Synchronized delta oscillations correlate with the resting-state functional MRI signal. *Proc Natl Acad Sci U S A*. 104:18265–18269.

Lu WY, Chen JY, Chang CF, Weng WC, Lee WT, Shieh JS. 2015. Multiscale entropy of electroencephalogram as a potential predictor for the prognosis of neonatal seizures. *PLoS One*. 10:e0144732.

Marinazzo D, Pellicoro M, Stramaglia S. 2008. Kernel method for nonlinear granger causality. *Phys Rev Lett*. 100: 144103.

Menon V. 2011. Large-scale brain networks and psychopathology: a unifying triple network model. *Trends Cogn Sci*. 15:483–506.

Menon V. 2015a. Large-scale functional brain organization. In: Toga AW, editor. *Brain mapping*. Waltham: Academic Press, pp. 449–459.

Menon V. 2015b. Salience network. In: Toga AW, editor. *Brain Mapping*. Waltham: Academic Press, pp. 597–611.

Menon V, Freeman WJ, Cutillo BA, Desmond JE, Ward MF, Bressler SL, Laxer KD, Barbaro N, Gevins AS. 1996. Spatio-temporal correlations in human gamma band electrocorticograms. *Electroencephalogr Clin Neurophysiol*. 98:89–102.

Menon V, Uddin LQ. 2010. Saliency, switching, attention and control: a network model of insula function. *Brain Struct Funct*. 214:655–667.

Miller KJ, Weaver KE, Ojemann JG. 2009. Direct electrophysiological measurement of human default network areas. *Proc Natl Acad Sci U S A*. 106:12174–12177.

MNI Open iEEG Atlas—Document Repository. URL: http://mni-open-ieegatlas.research.mcgill.ca (LAST ACCESSED 7 August 2019).

Murphy K, Birn RM, Handwerker DA, Jones TB, Bandettini PA. 2009. The impact of global signal regression on resting state correlations: are anti-correlated networks introduced? *NeuroImage*. 44:893–905.

Norman Y, Yeagle EM, Harel M, Mehta AD, Malach R. 2017. Neuronal baseline shifts underlying boundary setting during free recall. *Nat Commun*. 8:1301.

Ouyang G, Li X, Dang C, Richards DA. 2008. Using recurrence plot for determinism analysis of EEG recordings in genetic absence epilepsy rats. *Clin Neurophysiol*. 119:1747–1755.

Parvizi J, Kastner S. 2018. Promises and limitations of human intracranial electroencephalography. *Nat Neurosci*. 21: 474.

Pedersen M, Zalesky A, Omidvarnia A, Jackson GD. 2018. Multilayer network switching rate predicts brain performance. *Proc Natl Acad Sci U S A*. 115:13376–13381.

Pereda E, Quiroga RQ, Bhattacharya J. 2005. Nonlinear multivariate analysis of neurophysiological signals. *Prog Neurobiol*. 77:1–37.

Pincus SM. 2001. Assessing serial irregularity and its implications for health. *Ann N Y Acad Sci*. 954:245–267.

Popa D, Popescu AT, Pare D. 2009. Contrasting activity profile of two distributed cortical networks as a function of attentional demands. *J Neurosci*. 29:1191–1201.

Power JD, Cohen AL, Nelson SM, Wig GS, Barnes KA, Church JA, Vogel AC, Laumann TO, Miezin FM, Schlaggar BL *et al*. 2011. Functional network organization of the human brain. *Neuron*. 72:665–678.

Raccah O, Daitch AL, Kucyi A, Parvizi J. 2018. Direct cortical recordings suggest temporal order of task-evoked responses in human dorsal attention and default networks. *J Neurosci*. 38:10305–10313.

Richman JS, Moorman JR. 2000. Physiological time-series analysis using approximate entropy and sample entropy. *Am J Phys Heart Circ Phys*. 278:H2039–H2049.

Saxe GN, Calderone D, Morales LJ. 2018. Brain entropy and human intelligence: a resting-state fMRI study. *PLoS One*. 13:e0191582.

Schreiber T. 2000. Measuring information transfer. *Phys Rev Lett*. 85:461–464.

Schroeder CE, Lakatos P. 2009. Low-frequency neuronal oscillations as instruments of sensory selection. *Trends Neurosci*. 32:9–18.

Seeley WW, Menon V, Schatzberg AF, Keller J, Glover GH, Kenna H, Reiss AL, Greicius MD. 2007. Dissociable intrinsic connectivity networks for salience processing and executive control. *J Neurosci*. 27:2349–2356.

Sha Z, Wager TD, Mechelli A, He Y. 2019. Common dysfunction of large-scale neurocognitive networks across psychiatric disorders. *Biol Psychiatry*. 85:379–388.

Sokunbi MO, Fung W, Sawlani V, Choppin S, Linden DE, Thome J. 2013. Resting state fMRI entropy probes complexity of brain activity in adults with ADHD. *Psychiatry Res*. 214:341–348.

Sridharan D, Levitin DJ, Menon V. 2008. A critical role for the right fronto-insular cortex in switching between central-executive and default-mode networks. *Proc Natl Acad Sci USA*.. 105:12569–12574.

Supekar K, Menon V. 2012. Developmental maturation of dynamic causal control signals in higher-order cognition: a neurocognitive network model. *PLoS Comput Biol*. 8:e1002374.

Taghia J, Cai W, Ryali S, Kochalka J, Nicholas J, Chen T, Menon V. 2018. Uncovering hidden brain state dynamics that regulate performance and decision-making during cognition. *Nat Commun*. 9:2505.

Theiler J. 1986. Spurious dimension from correlation algorithms applied to limited time-series data. *Phys Rev A*. 34:2427–2432.

Uddin LQ. 2015. Salience processing and insular cortical function and dysfunction. *Nat Rev Neurosci*. 16:55–61.

UPENN-RAM. *UPENN-RAM RAM—Computational Memory Lab*. http://memory.psych.upenn.edu/RAM (last accessed 7 August 2019).

Wairagkar M, Hayashi Y, Nasuto SJ. 2018. Exploration of neural correlates of movement intention based on characterisation of temporal dependencies in electroencephalography. *PLoS One*. 13:e0193722.

Wang DJJ, Jann K, Fan C, Qiao Y, Zang YF, Lu H, Yang Y. 2018. Neurophysiological basis of multi-scale entropy of brain complexity and its relationship with functional connectivity. *Front Neurosci*. 12:352.

Wang MY, Wang J, Zhou J, Guan YG, Zhai F, Liu CQ, Xu FF, Han YX, Yan ZF, Luan GM. 2017. Identification of the epileptogenic zone of temporal lobe epilepsy from stereo-electroencephalography signals: a phase transfer entropy and graph theory approach. *Neuroimage Clin*. 16:184–195.

Wang Z, Li Y, Childress AR, Detre JA. 2014. Brain entropy mapping using fMRI. *PLoS One*. 9:e89948.

Watrous AJ, Tandon N, Conner CR, Pieters T, Ekstrom AD. 2013. Frequency-specific network connectivity increases underlie accurate spatiotemporal memory retrieval. *Nat Neurosci*. 16:349–356.

Xue SW, Yu Q, Guo Y, Song D, Wang Z. 2019. Resting-state brain entropy in schizophrenia. *Compr Psychiatry*. 89:16–21.

Yanagisawa T, Yamashita O, Hirata M, Kishima H, Saitoh Y, Goto T, Yoshimine T, Kamitani Y. 2012. Regulation of motor representation by phase–amplitude coupling in the sensorimotor cortex. *J Neurosci*. 32:15467–15475.

Zhou Y, Friston KJ, Zeidman P, Chen J, Li S, Razi A. 2018. The hierarchical organization of the default, dorsal attention and salience networks in adolescents and young adults. *Cereb Cortex*. 28:726–737.